ARTICLE

ACS chemical biology

Picomolar Inhibitors as Transition-State Probes of 5′-Methylthioadenosine Nucleosidases

Jemy A. Gutierrez[†,¶], Minkui Luo[†,¶], Vipender Singh[†], Lei Li[†], Rosemary L. Brown[‡], Gillian E. Norris[‡], Gary B. Evans[§], Richard H. Furneaux[§], Peter C. Tyler[§], Gavin F. Painter[§], Dirk H. Lenz[§], and Vern L. Schramm[†,*]

[†]Department of Biochemistry, Albert Einstein College of Medicine, Bronx, New York, 10461, [‡]Institute of Molecular Biosciences, Massey University, Private Bag 11222, Palmerston North, New Zealand, and [§]Carbohydrate Chemistry Team, Industrial Research Ltd., Lower Hutt, New Zealand. [¶]Contributed equally to this work.

ABSTRACT Transition states can be predicted from an enzyme's affinity to related transition-state analogues. 5′-Methylthioadenosine nucleosidases (MTANs) are involved in bacterial quorum sensing pathways and thus are targets for antibacterial drug design. The transition-state characteristics of six MTANs are compared by analyzing dissociation constants (K_d) with a small array of representative transition-state analogues. These inhibitors mimic early or late dissociative transition states with K_d values in the picomolar range. Our results indicate that the K_d ratio for mimics of early and late transition states are useful in distinguishing between these states. By this criterion, the transition states of *Neisseria meningitides* and *Helicobacter pylori* MTANs are early dissociative, whereas *Escherichia coli*, *Staphylococcus aureus*, *Streptococcus pneumoniae*, and *Klebsiella pneumoniae* MTANs have late dissociative characters. This conclusion is confirmed independently by the characteristic [1′-^{3}H] and [1′-^{14}C] kinetic isotope effects (KIEs) of these enzymes. Large [1′-^{3}H] and unity [1′-^{14}C] KIEs are observed for late dissociative transition states, whereas early dissociative states showed close-to-unity [1′-^{3}H] and significant [1′-^{14}C] KIEs. K_d values of various MTANs for individual transition-state analogues provide tentative information about transition-state structures due to varying catalytic efficiencies of enzymes. Comparing K_d ratios for mimics of early and late transition states removes limitations inherent to the enzyme and provides a better predictive tool in discriminating between possible transition-state structures.

Enzymes accelerate reactions by lowering the activation barriers for the formation of transition states. Transition-state theory suggests that the catalytic acceleration provided by an enzyme is proportional to the free energy released upon binding of transition-state analogues (*1, 2*). Stable transition-state analogue inhibitors that ideally mimic geometric and electrostatic features of a transition state are proposed to bind to the enzyme more tightly than substrate by a factor approaching the enzyme-imposed rate acceleration. Most enzymes have substrate Michaelis constant (K_m) values in the millimolar to micromolar range and catalytic accelerations on the order of $10^{10}-10^{15}$. Therefore, perfect transition-state analogues are expected to show dissociation constants (K_d) of $10^{-14}-10^{-23}$ M (*3*). The elucidation of transition-state structures therefore provides a blueprint for generating potent, tight-binding inhibitors. Conversely, probing enzymes with structurally diverse transition-state analogues can be a powerful tool to differentiate closely related isozymes by revealing the variations at their transition states. Isozymes are now known to exhibit characteristic transition-state structures, and comparing the structural differences among these transition states can provide valuable information for designing target-specific inhibitors (*4–7*).

Enzymatic transition states are difficult to probe because of their short lifetimes, the complications of enzyme matrix, and rate-limiting steps that are not involved with bond breaking or formation. The use of linear free energy relationships with an array of sub-

*Corresponding author, vern@aecom.yu.edu.

Received for review August 6, 2007 and accepted October 5, 2007.

Published online November 16, 2007

10.1021/cb700166z CCC: $37.00

© 2007 American Chemical Society

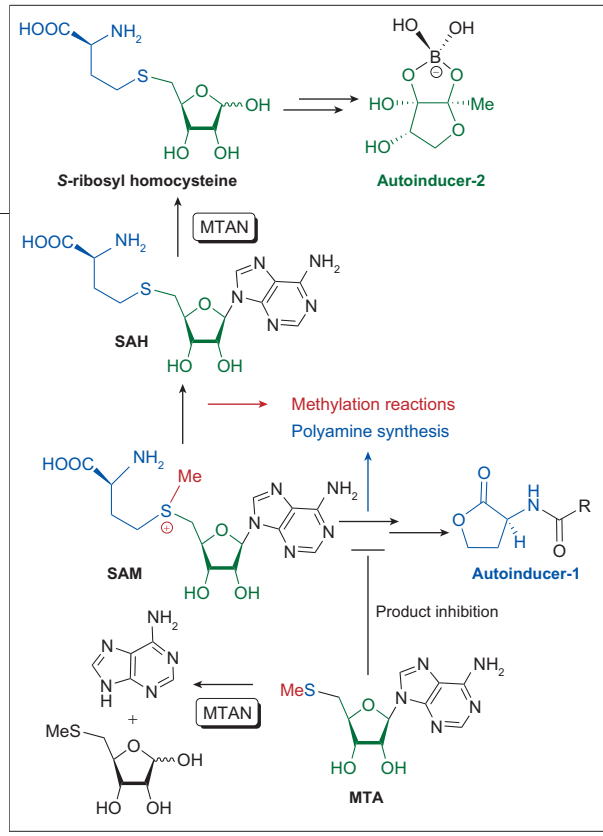

Figure 1. MTAN-linked metabolic pathways for purine salvage, quorum sensing, polyamine biosynthesis, and methylation reactions. Both MTA and SAH are MTAN substrates. For autoinducer-1 generation in bacterial quorum sensing and polyamine biosynthesis, the blue moiety of SAM serves as a precursor and MTA is the byproduct. The red moiety of SAM involves methylation reactions with SAH as byproduct. Inhibition of MTAN activities causes accumulation of SAH and MTA. These are proposed to downregulate methylation reactions and polyamine synthesis *via* product inhibition. The green moiety of SAM is a precursor for autoinducer-2 synthesis. The precursor for autoinducer-2 synthesis requires MTAN-mediated SAH degradation. The adenine moiety of SAH and MTA is recycled *via* MTAN-mediated hydrolyzis in the purine salvage pathway.

strates of different chemical reactivities and analysis of Brønsted coefficients has been successful in elucidating transition states for a number of enzymatic systems (*8, 9*) but is limited in providing detailed geometric properties of the transition states and requires that the enzyme be active on different substrates with altered pK_a's. Kinetic isotope effects (KIEs) provide another method for transition-state characterization and have been used to determine transition-state structures for many enzymatic reactions, with excellent accounts from Cleland and others (*4, 6, 10–14*). This method provides detailed geometric and electrostatic information on the transition-state structures in enzymatic or chemical reactions. Limitations of this method lie in the difficulty in obtaining isotopically labeled substrates and the requirement for highly precise measurements. Measurement of KIEs is also limited in enzymatic reactions where substrates bind irreversibly or chemical steps of the enzymes are rapid relative to rates of product release (*5, 7*). This work describes the use of transition-state analogues that mimic geometry and electrostatic features to predict the position of the transition state in the reaction coordinate, for a family of enzymes. By analyzing the dissociation constants of a small array of representative transition-state analogue inhibitors, differences in transition-state structures for the various enzymes are revealed.

5′-Methylthioadenosine nucleosidases (MTANs) are bacterial enzymes that belong to the *N*-ribosyl transferase family and catalyze the irreversible hydrolytic deadenylation reaction of 5′-methylthioadenosine (MTA) and *S*-adenosylhomocysteine (SAH) (Figure 1). 5′-Methylthioadenosine phosphorylase (MTAP) uses phosphorolysis instead of hydrolyzis to degrade MTA and is found in mammals. MTAN and MTAP are key enzymes in thiomethyl-group metabolism and are metabolically linked to *S*-adenosylmethionine (SAM)-related biological processes, such as quorum sensing (*15, 16*), methylation reactions (*17*), purine salvage, and polyamine biosynthesis (*18–20*). MTANs are involved in bacterial quorum sensing pathways by removal of the byproduct MTA for autoinducer-1 assembly or by generation of an autoinducer-2 precursor (Figure 1). These functions implicate MTANs as antibiotic targets (*21, 22*). Human MTAP regulates methylation reactions *via* the degradation of MTA (Figure 1), whose accumulation otherwise causes product inhibition (*17*). Human MTAP has also been suggested to be an anticancer target on the basis of its active involvement in purine salvage and polyamine biosynthesis (Figure 1) (*18, 19*).

Transition-state structures of *N*-ribosyl transferases that metabolize MTA can be either early or late dissociative, distinguished by the distances between the ribosyl anomeric carbon and the N9 of the adenine leaving group (Figure 2) (*4, 5, 23*). The transition-state analogue 5′-methylthio-Immucillin-A (MT-ImmA) resembles an early dissociative transition state, whereas 5′-methylthio-DADMe-Immucillin-A (MT-DADMe-ImmA) mimics a late dissociative transition state (Figure 2) (*24*). In this report, the MT-ImmA and MT-DADMe-ImmA inhibitor pair and related 5′-derivatives were used to probe the transition-state characteristics of several MTAN isozymes. These molecules are shown to be powerful inhibitors of MTANs, with dissociation constants in the picomolar range. In particular, the MT-ImmA and MT-DADMe-ImmA inhibitor pair reveals the nature of MTAN

transition states. This observation was confirmed by comparing their characteristic KIEs at the H1′ and C1′ positions. Our results indicate that these MTAN transition-state analogue inhibitors provide convenient probes for establishing the position of MTAN transition-state structures along the reaction coordinate.

RESULTS AND DISCUSSION

Discrimination of Transition States by MT-ImmA/DADMe-ImmA K_d ratio. The K_d's for MT-ImmA and MT-DADMe-ImmA by *Neisseria meningitides* MTAN were determined by inhibition studies with MTA as substrate (Figure 2). Both MT-ImmA and MT-DADMe-ImmA are slow-onset, tight-binding inhibitors of *N. meningitides* MTAN, with K_d values of 360 and 140 pM, respectively. Slow-onset inhibition is commonly observed for tight-binding transition-state analogue inhibitors and is consistent with inhibitor-induced conformational freezing. The K_d values of MT-ImmA and MT-DADMe-ImmA for *N. meningitides* MTAN are 10- to 100-fold larger than those for *Escherichia coli* MTAN (*24*), but approximately 10^2- to 10^3-fold smaller than those for *Streptococcus pneumoniae* MTAN (Table 1) (*22*). Compared to the ~10^5-fold magnitude variation in K_d of MT-ImmA and MT-DADMe-ImmA for the MTANs from *E. coli*, *S. pneumoniae*, and *N. meningitides*, the ratios of MT-ImmA K_d to MT-DADMe-ImmA K_d fall into only two categories, with near unity for *N. meningitides* MTAN and approximately 10^2 for *S. pneumoniae* and *E. coli* MTANs.

The K_d ratios for the bacterial MTANs from *Staphylococcus aureus*, *Klebsiella pneumoniae*, and *Helicobacter pylori* were also measured to establish if MTANs from other species exhibit profiles similar to the K_d ratios with MT-ImmA and MT-DADMe-ImmA. The K_d ratios for these enzymes fall into the same two categories, with near unity for *H. pylori* MTAN and around 10^2 for *S. aureus* and *K. pneumoniae* MTANs (Figure 2 and Table 1).

The two well-defined K_d ratios of the MT-ImmA and DADMe-ImmA inhibitor pair among the tested MTANs (Table 1) suggest that this approach can differentiate between transition-state structures of MTAN isozymes. Geometric differences between MT-ImmA and MT-DADMe-ImmA reflect the variation in adenine-ribosyl bond distances at MTAN transition states. The 2.5 Å distance between the 1′-pyrrolidine cation and the C9 of 9-deazaadenine in MT-DADMe-ImmA mimics fully dissociative transition states for MTANs, for which the ribosyl-adenine distance is 3 Å or greater. The shorter distance

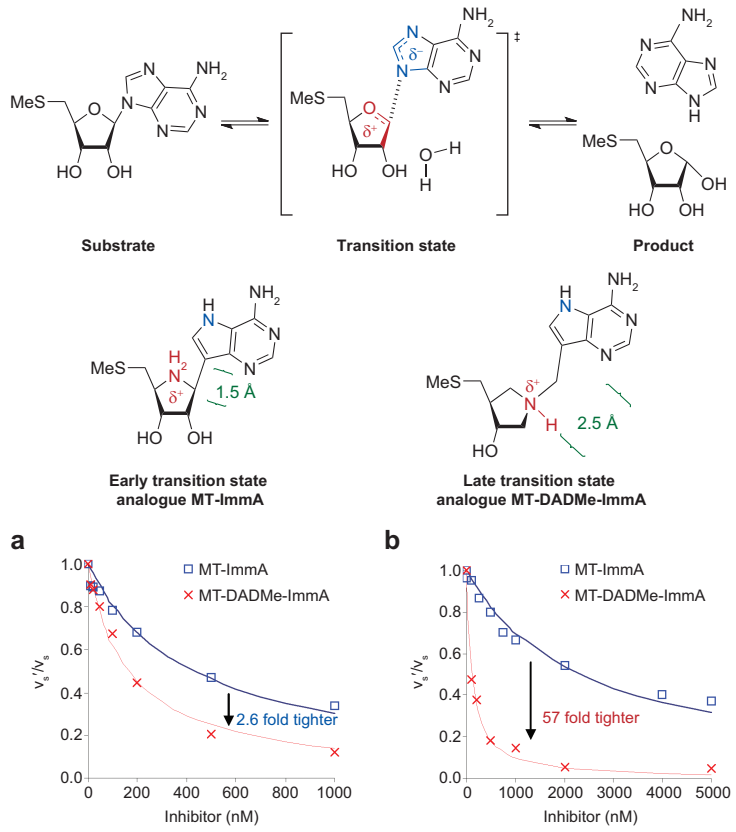

Figure 2. MTAN-catalyzed MTA hydrolysis and its inhibition by the early dissociative transition-state analogue MT-ImmA and by the late dissociative transition-state analogue MT-DADMe-ImmA. Distinct features of the transition states and the analogues are highlighted. The dissociation constants for MT-ImmA and MT-DADMe-ImmA were obtained as described in METHODS. a) *N. meningitides* MTAN, characterized by its inhibition profile as an early dissociative transition state. b) *K. pneumoniae* MTAN, characterized by its inhibition profile as a late dissociative transition state.

of 1.5 Å between C1′ and C9 of 9-deazaadenine in MT-ImmA makes the molecule resemble early dissociative MTAN transition states (Figure 2 and Figure 3). The K_d ratio for the pair of inhibitors (Figure 2 and Table 1) therefore reflects the early or late dissociative nature of MTAN transition states. This analysis concludes that *N. meningitides* and *H. pylori* MTANs adopt early dissociative transition states, whereas the transition states of *E. coli*, *S. aureus*, *S. pneumoniae*, and *K. pneumoniae* MTANs are late dissociative.

[1′-^{3}H], [1′-^{14}C] KIEs and Transition-State Characters of MTANs. Early and late dissociative transition-state characters can be distinguished by

TABLE 1. Dissociation constants of MT-, EtT-, BnT-, and *p*-ClPhT-ImmA/DADMe-ImmA inhibitors with MTANs and MTAP[a]

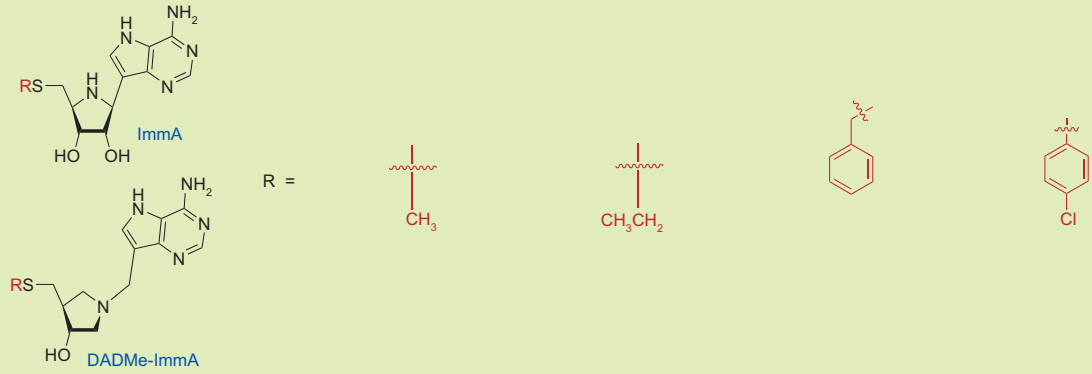

MTANs[b]	5′-R[c,d]	Me- K_d (pM)	Me- $\frac{K^{ImmA}}{K^{DADMe}}$	Et- K_d (pM)	Et- $\frac{K^{ImmA}}{K^{DADMe}}$	Bn- K_d (pM)	Bn- $\frac{K^{ImmA}}{K^{DADMe}}$	*p*-ClPh- K_d (pM)	*p*-ClPh- $\frac{K^{ImmA}}{K^{DADMe}}$
N. meningitides[e,f]	ImmA	360	**2.6**	120	**2.6**	170	**7.1**	63	**3.0**
	DADMe	140		46		24		21	
H. pylori[e,f]	ImmA	1.2×10^3	**2.1**	3.4×10^3	**6.6**	2.0×10^5	**1.0**	4.0×10^4	**70**
	DADMe	571		515		2.0×10^5		570	
K. pneumoniae[e,g]	ImmA	4.5×10^4	**57**	1.3×10^4	**5.9**	1.3×10^4	**6.8**	4.1×10^3	**8.2**
	DADMe	784		2.2×10^3		1.9×10^3		500	
S. aureus[e,g]	ImmA	7.7×10^4	**55**	1.2×10^4	**9.2**	1.2×10^4	**14**	5.3×10^4	**6.6**
	DADMe	1.4×10^3		1.3×10^3		841		8×10^3	
E. coli[g,h]	ImmA	77	**38**	27	**28**	12	**26**	2	**43**
	DADMe	2		0.95		0.46		0.047	
S. pneumoniae[g,h]	ImmA	1.0×10^6	**42**	4.0×10^4	**4.0**	2.1×10^5	**86**	1.9×10^5	**536**
	DADMe	2.4×10^4		1.0×10^4		2.4×10^3		360	
Human MTAP[g,h]	ImmA	1.0×10^3	**12**	266	**7.8**	2.6×10^4	**37**	166	**17**
	DADMe	86		34		700		10	

[a] K_d determination was done as described in METHODS. [b] Entries are for MTANs from various bacterial species except the last entry, which is for human MTAP. [c] The 5′-substituents for ImmA and DADMe-ImmA inhibitors are shown above. [d] All K_d ratios are reported as $K^{ImmA}/K^{DADMe\text{-}ImmA}$. [e] Dissociation constants for these inhibitors are first reported here. [f] Early dissociative transition states (red). [g] Late dissociative transition states (blue). [h] Reported dissociation constants from references (*23*, *24*, *28*).

their characteristic [1′-^{3}H] and [1′-^{14}C] KIEs (*4*–*7*). The [1′-^{3}H] and [1′-^{14}C] KIEs of *N. meningitides* (*32*), *S. pneumoniae*, and *E. coli* MTANs have been measured (Table 2) (*4*, *5*). In addition, we measured the [1′-^{3}H] and [1′-^{14}C] KIEs of *H. pylori*, *S. aureus*, and *K. pneumoniae* MTANs (Table 2). For *N*-ribosyl transferase enzymes, unity [1′-^{14}C] and large [1′-^{3}H] KIEs correspond to late dissociative transition states, whereas significant [1′-^{14}C] KIEs with small [1′-^{3}H] KIEs are expected for early dissociative transition states (*5*, *25*). Alternatively, the transition-state characters of MTANs were examined by comparing the ratio of $[^{14}(V/K) - 1]/[^3(V/K) - 1]$. Northrop showed that assuming there was no equilibrium isotope effect, comparing the ratio of $^x(V/K) - 1$ instead of $^x(V/K)$ allows the evaluation of isotope effects without the need to correct for forward commitments (*26*) (see footnote *f* in Table 2). The $(V/K) - 1$ ratios were shown to be 0.2–1.3 for early dissociative transition states and 0–0.02 for late dissociative transition states, respectively (Table 2). The efficiency of the latter approach was validated by including the KIEs of other *N*-ribosyl transferase enzymes with known transition-state structures as controls (Table 2).

The characteristic [1′-^{3}H] and [1′-^{14}C] KIEs indicate that the transition states of *N. meningitides* and *H. pylori* MTANs are early dissociative, whereas those of *E. coli*, *S. aureus*, *S. pneumoniae*, and *K. pneumoniae* MTANs are late dissociative (Table 2). These results are in good agreement with the reported transition-state structures of *S. pneumoniae*, *E. coli*, and *N. meningitides* MTANs that have been solved through computational modeling and complete KIE analysis (*4*, *5*, *32*). *S. pneumoniae* and *E. coli* MTANs adopt late dissociative transition states (Figure 3) with C1′–N9 distances of 3.0 Å or greater (*8*, *9*, *21*). In contrast, the transition state of *N. meningitides* MTAN shows an early dissociative

character with a short C1′—N9 of 1.68 Å (*32*) (Figure 3). The molecular electrostatic potential (MEP) surfaces of early and late dissociative transition-state structures were compared to those of MT-ImmA and MT-DADMe-ImmA (Figure 3). Very prominent is the cationic C1′ of the *E. coli* transition state (indicated by an arrow, Figure 3), which is mimicked well by the 1′-pyrolidine nitrogen of MT-DADMe-ImmA and 4′ iminoribitol nitrogen of MT-ImmA. The overall MEP and geometry of MT-ImmA, however, resembles an early dissociative MTAN transition state, whereas the MEP and geometry of MT-DADMe-ImmA better represents the late dissociative state. These results are fully consistent with the proposed transition states derived from the K_d ratios.

Interestingly, despite other potential transition states for the MTAN reaction, only early and late dissociative transition states have been observed for those previously solved using KIEs (e.g., *E. coli*, *S. pneumoniae*, and *N. meningitides*). In addition, screening of libraries of inhibitors carrying various functionalities at different positions revealed that the analogues with highest affinities for MTANs described here are those that mimic the early and late dissociative transition states presented in this work. The observation of this binary system was a curious one, supported by KIE results at the 1′ position.

Structural Rationale for Picomolar Affinity to Transition-State Analogues. Crystal structures of *S. pneumoniae* and *E. coli* MTAN bound by MT-ImmA and MT-DADMe-ImmA reveal several key features for the nanomolar to picomolar affinities of these analogues (Figure 4) (*22, 27*). The N6 and N1 of MT-ImmA and MT-DADMe-ImmA 9-deazaadenines are within hydrogen bond distances of neighboring MTAN residues, and the 5′-methylthio groups are docked in a hydrophobic binding pocket (Figure 4) (*22, 27*). The hydroxyl groups of MT-ImmA and MT-DADMe-ImmA form hydrogen bonds with Glu174 or a bridging water. The cationic 4′-iminoribitol nitrogen of ImmA and 1′-pyrrolidine nitrogen of DADMe-ImmA mimic the cationic C1′ at the transition states. Electrostatic interaction between these cations and an immobilized nucleophilic water (or hydroxide) resembles the nucleophile-stabilized MTAN transition state. Ion pair formation in a relatively hydrophobic environment can release up to 10 kcal/mol stabilization energy (Figure 2). In addition, the high pK_a at N7 for these inhibitors provides an N-H imino hydrogen bond donor compared to an N7 hydrogen bond acceptor for the substrate MTA. As C-N bond cleavage of MTA progresses toward the transition state, the pK_a of N7 increases and can be protonated at the transition state (*22, 27*). These structural features of MT-ImmA and MT-DADMe-ImmA-derived inhibitors can rationalize up to 10^5-fold increased affinities relative to the substrate.

Preferential Affinity for DADMe-ImmA Relative to ImmA Inhibitors. All MTANs show better affinity for late dissociative transition-state analogue inhibitors (DADMe-ImmAs) relative to early dissociative transition-state analogue inhibitors (ImmAs) (Table 1). However, the ratio of ImmAs to DADMe-ImmAs affinity differs for these transition-state features. For example, *N. meningitides* MTAN binds MT-DADMe-ImmA 2.7-fold better than MT-ImmA in spite of its early dissociative transition state. DADMe-ImmA inhibitors have a fully protonated 1′-pyrrolidine nitrogen (pK_a = *9.2*) at physiological pH of 7.4 relative to less protonated 4′-iminoribitol nitrogen (pK_a ≈ *6.9*) of ImmA inhibitors (*22, 24, 28*). The lack of the 2′-hydroxyl moiety in DADMe-ImmA inhibitors is proposed to permit a closer formation of the ion pair at all MTAP catalytic sites (*22, 24, 28*). These factors allow DADMe-ImmA inhibitors to better capture total MTAN transition-state binding energy and thus account for their overall higher affinity. However, the late dissociative transition states of *E. coli*, *S. aureus*, *S. pneumoniae*, and *K. pneumoniae* MTANs exhibit a 38- to 57-fold preference for MT-DADMe-ImmA relative to MT-ImmA. In contrast, the early dissociative character of *N. meningitides* and *H. pylori* MTAN transition states is reflected by only a 2.1- to 2.6-fold preference for MT-DADMe-ImmA (Table 1).

Effects of 5′-Substituents on MTAN Inhibitors. Both MTA and SAH are MTAN substrates (*15*). Given the structural difference between homocysteine and methylthio

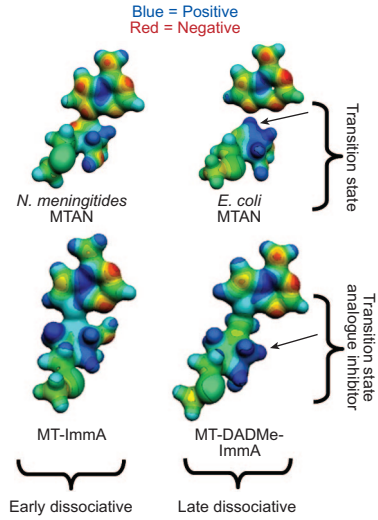

Figure 3. Molecular electrostatic potentials (MEPs) of an early dissociative MTAN transition state, a late dissociative MTAN transition state, MT-ImmA, and MT-DADMe-ImmA. The MEPs were plotted at 0.15 e/Å^3 with geometry optimization at the B3LYP/6-31G(d,p) level of theory. The structures of *E. coli* and *N. meningitides* ((*32*)) MTAN transition states exemplify late and early dissociative transition states with *N*-ribosidic bond distances of 3.0 and 1.68 Å, respectively (*5*). The MEPs of early dissociative transition-state analogue MT-ImmA and late dissociative transition-state analogue MT-DADME-ImmA are shown for comparison. The arrows indicate partial positive charge around C1′ of the *E. coli* transition state, mimicked at the 1′-pyrolidine nitrogen of MT-DADMe-ImmA and 4′-iminoribitol nitrogen of MT-ImmA.

TABLE 2. Catalytic efficiency and experimental KIEs of MTANs and other *N*-ribosyl transferase enzymes[a]

Enzymes[b]	Transition-state characters[c]	Catalytic efficiency and experimental KIEs[d]			
		k_{cat}/K_m ($M^{-1}s^{-1}$)[e]	[1′-^{14}C] KIE	[1′-^{3}H] KIE	$\frac{^{14}(V/K)-1}{^{3}(V/K)-1}_f$
N. meningitides MTAN	Early $D_N^{\ddagger}*A_N$[g]	2.9×10^5	1.039 ± 0.006	1.030 ± 0.010	1.3
H. pylori MTAN	Early $D_N^{\ddagger}*A_N$[g]	1.3×10^6	1.007 ± 0.004	1.036 ± 0.004	0.2
Bovine PNP	Early $D_N^{\ddagger}*A_N$[h]	N.A.	1.026 ± 0.006	1.141 ± 0.004	0.2
K. pneumoniae MTAN	S_N1[g]	1.7×10^6	1.000 ± 0.001	1.094 ± 0.005	0
S. aureus MTAN	S_N1[g]	2.0×10^6	1.001 ± 0.004	1.122 ± 0.005	1×10^{-2}
E. coli MTAN	S_N1[i]	4.7×10^7	1.004 ± 0.003	1.160 ± 0.004	2×10^{-2}
S. pneumoniae MTAN	S_N1[j]	1.1×10^4	1.000 ± 0.005	1.235 ± 0.002	0
Human PNP	S_N1[k]	N.A.	1.002 ± 0.006	1.184 ± 0.004	1×10^{-2}

[a]Values of k_{cat}/K_m, [1′-^{3}H] KIEs, and [1′-^{14}C] KIEs were determined as described in METHODS. [b]All enzymes belong to the *N*-ribosyl transferase family. [c]Early $D_N^{\ddagger}*A_N$ stands for early dissociative transition state (*31*) and S_N1 for late or fully dissociative transition state (*5*). [d][1′-^{3}H] KIEs were measured with [5′-^{14}C]MTA as remote control. The KIE of the latter is expected to be unity because the labeled position is four bonds away from the reaction center. [1′-^{14}C] KIEs were obtained upon correcting reference KIEs of [4′-^{3}H]MTA, which was used as remote control. [e]Only k_{cat}/K_m values of MTANs are shown for comparison. $f\frac{^{14}(V/K)-1}{^{3}(V/K)-1} = \frac{k-1}{^{3}k-1}$ can be derived on the basis of $^{x}(V/K) = \frac{^{x}k+C_f}{1+C_f}$ (*4, 6, 10, 11*), where ^{x}k is the intrinsic KIE of a labeled heavy atom (^{14}C or ^{3}H), and C_f is forward commitment factor. Comparing the ratio of $^{x}(V/K) - 1$ instead of $^{x}(V/K)$ avoids the correction of forward commitment factor because using $^{x}(V/K)$ or ^{x}k gives the same result based on the analysis above (*26*). [g]Determined in ref *32*. [h]From ref *7*. [i]From ref *24*. [j]From ref *22*. [k]From ref *6*.

groups, this specificity for the 5′-position of MTAN substrates requires an adaptable binding region to accommodate the different 5′-residues. The K_d ratios of 5′-R-ImmA/5′-R-DADMe-ImmA inhibitor pairs (R = MT, EtT, BnT, and *p*-ClPhT) were compared to examine the 5′-specificity of the transition-state analogue inhibitors (Table 1). The K_d ratios among the different 5′-substitutes are similar for *N. meningitides* and *E. coli* MTANs (Table 1). However, MTANs from *H. pylori*, *S. aureus*, *S. pneumoniae*, and *K. pneumoniae* showed wide variation of the K_d ratios with the largest difference being 130-fold for *S. pneumoniae* MTAN. For *H. pylori* MTAN, the K_d ratios of EtT- and BnT-ImmA/DADMe-ImmA inhibitor pairs are similar to that of MT-ImmA/DADMe-ImmA pair (6.6 and 1.0 *vs* 2.1), whereas the K_d ratio for the *p*-ClPhT- inhibitor was 70. With *S. pneumoniae* MTAN, MT-, BnT-and *p*-ClPhT-ImmA/DADMe-ImmA pairs exhibited enhanced K_d ratios of 42, 86, and 536, respectively. These values are 10- to 10^2-fold greater than that for the EtT-ImmA/EtT-DADMe-ImmA pair. *S. aureus* and *K. pneumoniae* MTANs have the highest K_d ratios of 55 and 57, respectively, for the MT-ImmA/MT-DADMe-ImmA pair. Other thiol substituents for inhibitors of *S. aureus* and *K. pneumoniae* MTANs provide less discrimination in the K_d ratio (Table 1).

Crystal structures of *S. pneumoniae* and *E. coli* MTANs bound by MT-ImmA and MT-DADMe-ImmA reveal that the 5′-methylthio residues of the two inhibitors are buried in hydrophobic binding pockets (Figure 4) (*24, 27*). Structural flexibility of the binding pockets accounts for the 5′-specificity for MTAN substrates and the affinity of 5′-substituted ImmA- and DADMe-ImmA-derived inhibitors (Table 1). Of the six MTANs in Table 1, only the K_d ratios of *N. meningitides* and *E. coli* MTANs are not strongly affected by the 5′-substituents. Thus, bulky 5′-substituents in ImmA/DADMe-ImmA inhibitor pairs do not affect their ability to distinguish the transition states of *N. meningitides* and *E. coli* MTANs (Table 1). Consequently, the size and compatibility of the 5′-group binding pockets of *N. meningitides* and *E. coli* MTANs can be probed by directly comparing the K_d values of MT-, EtT-, BnT-, and *p*-ClPhT-ImmA/DADMe-ImmA inhibitors.

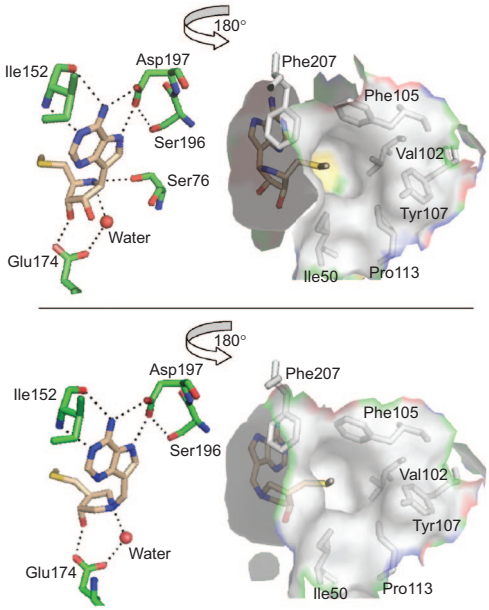

Figure 4. Crystal structures of *E. coli* MTAN bound to the transition-state analogue inhibitors MT-ImmA and MT-DADMe-ImmA (*27*). Figures for MT-ImmA-bound MTAN (upper) and MT-DADMe-ImmA-bound MTAN (lower) were generated from PDB files 1Y6R and 1Y6Q, respectively. Structures were rotated 180° to highlight the key residues for transition-state stabilization (left) and the hydrophobic binding pocket for inhibitor 5′-moiety (right). Color images were generated using PyMOL v0.99 (DeLano Scientific, LLC).

The K_d values for both ImmA and DADMe-ImmA inhibitors decrease 6-fold for *N. meningitides* MTAN and 40-fold for *E. coli* MTAN as the sizes of 5′-substituents are increased from MT to the *p*-ClPhT groups. The magnitude of affinity enhancement (K_d reduction) is less than expected for an entropy-driven hydrophobic effect, where each methylene is expected to contribute −0.8 kcal/mol (4-fold) to binding affinity (*29*). However, tighter binding with larger hydrophobic 5′-groups is consistent with the hydrophobic and relatively vacant space of the 5′- binding pocket revealed in MTAN crystal structures (Figure 4). Consequently, increased hydrophobicity of the 5′-group enhances their binding affinity by optimizing the hydrophobic interactions with the enzymes.

Different from *N. meningitides* and *E. coli* MTANs, *H. pylori*, *S. aureus*, *S. pneumoniae*, and *K. pneumoniae* MTANs show the altered K_d ratios when they bind to bulky 5′-derivatives larger than the MT group of MTA (Table 1). The variation in K_d ratios argues that 5′ bulky substitiuents on MT-ImmA and MT-DADMe-ImmA diminish their ability to distinguish early and late dissociative transition states of these MTANs. Consequently, EtT-, BnT-, and *p*-ClPhT-ImmA and DADMe-ImmA inhibitors are useful probes for examining the 5′-specificity for MTAN substrates but not for discriminating early from late transition states. The K_d ratios for EtT-, BnT-, and p-ClPhT-ImmA/DADMe-ImmA inhibitor pairs mainly report the transition-state structures with EtT-, BnT- , and p-ClPhT-adenosine as substrates, respectively. The utility of the MT-ImmA/MT-DADMe-ImmA inhibitor pair results from their similarity to MTAN transition states with MTA as the substrate and minimal contributions from the extended 5′-hydrophobic binding site. This observation suggests that even slight structural variations in the substrate can result in a significant change in the transition state.

Using Transition-State Analogues To Probe Enzymatic Transition States. Binding affinity of transition-state analogue inhibitors is determined by the degree of similarity between transition state and analogues, as well as the catalytic rate acceleration imposed by individual MTANs. The k_{cat}/K_m values of the six MTANs vary from 4.7×10^7 M^{-1} s^{-1} for *E. coli* MTAN to 1.1×10^4 M^{-1} s^{-1} for the *S. pneumoniae* enzyme (Table 2). Varied catalytic efficiency makes it impossible to directly relate the K_d value of transition-state analogue inhibitors to transition-state structure. For instance, *N. meningitides* MTAN shows 100-fold higher affinity to MT-DADMe-ImmA compared to *S. pneumoniae* MTAN, even though it is the latter that acts through a late dissociative transition state (*4*). The affinity of *S. pneumoniae* MTAN for the late dissociative transition-state analogue MT-DADMe-ImmA is masked by poor catalytic efficiency compared to that of *N. meningitides* MTAN ($k_{cat}/K_m = 1.1 \times 10^4$ *vs* 2.9×10^5 M^{-1} s^{-1}, Table 2). Differences in catalytic efficiency of MTAN isozymes are eliminated by the use of K_d ratios with early and late transition-state mimics.

A similar approach for transition-state discrimination can be applied to other *N*-ribosyl transferase enzymes, such as purine nucleoside phosphorylases (PNPs) and MTAP, whose transition states also involve dissociation of the *N*-ribosidic bond (*30*). For human and bovine PNPs (HsPNP and BtPNP, respectively), the K_d ratios for the ImmH and DADMe-ImmH inhibitor pair are 3.5 for the late dissociative HsPNP and 0.2 for the early disso-

ciative BtPNP. The 17-fold difference in the K_d ratios for early and late dissociative PNP transition states is consistent with this approach to characterize MTANs using the MT-ImmA and MT-DADMe-ImmA inhibitor pair (Table 1). Thus, PNP transition states can also be probed with the K_d ratio of early and late PNP transition-state mimics.

Human MTAP adopts a late dissociative transition state with a K_d ratio of 12 using the MT-ImmA/MT-DADMe-ImmA inhibitor pair (*19, 23*). It would be interesting to find an MTAP isozyme that had an early dissociative transtition state and evaluate the K_d ratio for the current array of inhibitor pairs. If it fell within 0.6–0.7 for the MT-ImmA/MT-DADMe-ImmA inhibitor pair, that would suggest that the ~20-fold difference in ratios for late and early dissociative transition states observed for MTANs and PNPs may be a more general theme for *N*-ribosyl transferases. In addition, the relatively consistent K_d ratios among MT-, EtT-, BnT-, and *p*-ClPhT-ImmA/DADMe-ImmA inhibitor pairs for human MTAP also makes these inhibitors suitable for examining inhibitor 5′-binding compatibility, similar to that shown above for *N. meningitides* and *E. coli* MTANs (Table 1).

Conclusions. The dissociation constants of MT-, EtT-, BnT-, and *p*-ClPhT-ImmA and -DADMe-ImmA inhibitors were compared for *S. pneumoniae*, *E. coli*, *N. meningitides*, *H. pylori*, *S. aureus*, and *K. pneumoniae* MTANs. Most inhibitors showed slow-onset, tight binding with picomolar K_d values. MT-ImmA and MT-DADMe-ImmA resemble early and late dissociative MTAN transition states, respectively, but the K_d values vary significantly among the MTANs. This variation stems from different catalytic efficiencies. Comparison of the K_d ratios for the MT-ImmA/MT-DADMe-ImmA inhibitor pair serves as a reliable indication of early and late dissociative MTAN transition states. This approach indicates that the transition states of *N. meningitides* and *H. pylori* MTANs are early dissociative, whereas those of *E. coli*, *S. aureus*, *S. pneumoniae*, and *K. pneumoniae* MTANs are late dissociative. The same conclusion has been reached independently by comparing the characteristic [1′-^{3}H] and [1′-^{14}C] KIEs of these enzymes. The K_d ratios of transition-state-mimicking inhibitors provides a convenient approach to probe transition-state structures and inhibitor 5′-binding specificity of various MTANs. This approach is readily applied to other *N*-ribosyl transferases. In summary, we have documented an inhibitor-based approach to probe transition-state structures through a small array of transition-state analogue inhibitors.

METHODS

Reagents and Materials. [1′-^{3}H]Ribose, [1′-^{14}C]ribose, [6′-^{14}C]glucose, and [5′-^{3}H]glucose were purchased from American Radiolabeled Chemicals, Inc. Hexokinase, glucose-6-phosphate dehydrogenase, phosphogluconic acid dehydrogenase, L-glutamic dehydrogenase, phosphoriboisomerase, adenylate kinase (AK), and pyruvate kinase (PK) were purchased from Sigma. Phospho-D-ribosyl-1-pyrophosphate (PRPP) synthase, adenine phosphoribosyltransferase (APRTase), ribokinase (RK), SAM synthetase, *E. coli* MTAN, and *S. pneumoniae* MTAN were purified according to the reported methods (*4, 5, 10, 11, 23*). All ImmA and DADMe-ImmA inhibitors were prepared according to published procedures (*18, 19*). Inhibitor concentrations were obtained from the absorbance at 274 nm with extinction coefficient of 8.5 mM^{-1} cm^{-1} for 9-deazaadenine moiety. The other reagents were obtained from readily available commercial sources and used without further purification.

Expression of *N. meningitides*, *H. pylori*, *S. aureus*, and *K. pneumoniae* MTANs. The MTAN gene sequences from *N. meningitides* MC58 and *H. pylori* J99 were amplified from genomic DNA (ATCC) and cloned into a modified pET-32 vector to direct high-level expression of MTAN with a noncleavable N-terminal His_6 tag. Cultures (1.5 L) of BL21(DE3) harboring MTAN constructs were induced with 0.5 mM IPTG for 20 h at 25 °C with vigorous shaking. Cell pellets were washed and lysed in 40 mL of lysis buffer (25 mM HEPES, 0.5 M NaCl, 10 mM imidazole, pH 7.6, protease inhibitors, and 0.25 mM TCEP) with the use of a high pressure cell disrupter set at 15K psi. After removal of cell debris by centrifugation, the soluble cell lysates were loaded onto nickel-charged chelating sepharose (GE Healthcare) and washed with lysis buffer containing 20–150 mM imidazole. The His_6-MTANs were eluted in 250 mM imidazole, desalted using a Sephadex G-15 (GE Healthcare) gel filtration column, equilibrated with low salt buffer (100 mM HEPES, 30 mM KCl, pH 7.6), and concentrated to 40 mg mL^{-1}.

Purified His_6-MTAN proteins from *S. aureus* and *K. pneumoniae* were found to have limited solubility. MTAN sequences from these species were therefore expressed in pProEx-HTb (Invitrogen) to permit proteolytic removal of the His tag. Recombinant fusion protein was prepared as described above, bound to a 5-mL HP His trap column (GE Healthcare), and then eluted in 30 mL of buffer containing 250–350 mM imidazole. The fusion protein was equilibrated with rTEV buffer (100 mM HEPES, 30 mM KCl, 1 mM DTT, pH 7.6) and incubated with rTEV protease for 1 h at RT then overnight at 4 °C. A white precipitate consisting mainly of uncleaved protein and the fusion tag was removed by centrifugation and filtration. The filtrate was passed through a 5-mL HP His trap column. Fractions containing pure cleaved MTAN were equilibrated with low salt buffer and concentrated to 40–70 mg mL^{-1}. SDS-PAGE analysis of each of the purified MTANs revealed single bands of pure protein of approximately 26 kDa. Protein concentrations were determined by both the absorbance at 280 nm and Bradford assay with BSA as standard.

Synthesis of Isotopically Labeled MTAs. [1′-^{3}H]MTA, [1′-^{14}C]MTA, [4′-^{3}H]MTA, and [5′-^{14}C]MTA were prepared from [1′-

^{3}H]ribose, [1′-^{14}C]ribose, [5′-^{3}H]glucose, and [6′-^{14}C]glucose, respectively, *via* three processes of conversion as reported previously (*4, 5, 23*). Briefly, for conversion from ribose to ATP, 2 mM adenine and 1 mM ribose (final concentrations) were added into a solution containing 20 mM phosphoenolpyruvate, 0.1 mM ATP, 100 mM phosphate, 50 mM glycylglycine, 50 mM KCl, 20 mM $MgCl_2$, and 2 mM DTT (pH = 7.4). The reaction was initialized by the addition of an enzyme stock containing 0.01 unit RK, 0.01 unit APRTase, 0.01 unit PRPP synthase, 1 unit AK, and 1 unit PK. The mixture was incubated at 37 °C for 12 h to generate radiolabeled ATPs. The isotopically labeled ATPs were then purified by reverse phase HPLC (50 mM triethylammonium acetate, pH = 5.0, 1 mL min^{-1}, retention time = 12 min). This sample was lyophilized overnight and then subjected to another reverse phase HPLC (4% (v/v) MeOH/H_2O, 1 mL min^{-1}, retention time = 5 min). Solvent was removed by lyophilization to give ATPs with 98% yield on the basis of starting ribose.

For conversion from glucose to ATP, the reaction buffer contained 2 mM adenine and 1 mM glucose or glucose 1-phosphate, 20 mM phosphoenolpyruvate, 0.1 mM unlabeled ATP, 100 μM β-NADP sodium salt, 20 mM α-keto-glutarate, 5 mM NH_4Cl, 100 mM phosphate, 50 mM glycylglycine, 50 mM KCl, 20 mM $MgCl_2$, and 2 mM DTT (pH = 7.4), 1 unit hexokinase, 1 unit glucose-6-phosphate dehydrogenase, 0.075 unit phosphogluconic acid dehydrogenase, 1 unit L-glutamate dehydrogenase, 0.05 unit phosphoriboisomerase, 0.2 unit APRTase, 0.015 unit PRPP synthase, 1 unit AK, and 1 unit PK. The reaction was incubated at 37 °C for 12 h, and the isotopically labeled ATPs were purified similarly as described above (60–70% yield on the basis of glucose).

For MTA generation, isotopically labeled ATP were first converted to SAM in a 1-mL reaction mixture containing 100 mM Tris (pH = 7.9), 50 mM KCl, 20 mM $MgCl_2$, 7% β-mercaptoethanol, 10 mM methionine, 1 unit of inorganic pyrophosphatase, and ~0.1 unit of SAM synthetase. The reactions were completed in 6 h with 90–95% yield. SAM was subsequently converted to MTA by acid hydrolyzis at 75 °C for 3.5 h (pH = 3 by adding 100 μL of 1 M citrate buffer, 75% yield). MTA was purified by reverse phase HPLC with 25% (v/v) methanol in water as eluting solvent. Purified MTAs were lyophilized and stored at −80 °C before use.

Enzyme Activity Assays, and Measurement of Dissociation Constants. MTAN activities were assayed as reported previously (*22, 24*). Briefly, all experiments were carried out at 25 °C, in 1 mL total reaction volume containing 100 mM HEPES buffer, pH 7.5, and 50 mM KCl with MTA as substrate. Kinetic constants (k_{cat} and K_m) were determined by monitoring MTA hydrolyzis at 274 nm where $\Delta\epsilon_{MTA} = 1.6$ mM^{-1} cm^{-1}. To determine K_d of inhibitors, a xanthine oxidase-coupled assay was carried out. Saturating levels of MTA (1–2 mM) and various concentrations of inhibitor were mixed with xanthine oxidase (0.5 unit mL^{-1}), which is used to convert the product adenine to 2,8-dihydroxyadenine ($\Delta\epsilon_{2,8\text{-dihydroxadenine}} = 15.2$ mM^{-1} cm^{-1} at 293 nm). Reactions were initiated by the addition of 8–10 nM MTAN, and absorbance at 293 nm was monitored. Control experiments were carried out in the absence of either inhibitor or MTAN. Slow onset dissociation constants K_d in the presence of >10-fold excessive inhibitor were obtained using the following equation:

$$v_s'/v_s = \frac{K_m + [S]}{K_m + [S] + K_m[I]/K_d}$$

where v_s' and v_s are steady-state rates in the presence and absence of inhibitor, respectively; K_m is substrate Michaelis constant, which was obtained as described above; and [S] and [I] are the concentrations of the substrate MTA and inhibitor, respectively. If the concentration of inhibitor is <10-fold the concentration of enzymes, the following correction was then applied:

$$I' = I - (1 - v_0'/v_0)E_t \quad (2)$$

where I' is the effective inhibitor concentration; I is the concentration of inhibitor used in the assay; v_0' and v_0 are initial rates in the presence and absence of inhibitor, respectively; and E_t is total MTAN concentration used in the assay. All data fitting was carried out with KaleidaGraph, ver. 3.5 (Synergy Software).

Determination of KIEs by Isotope Ratio Analysis. [1′-^{14}C] and [1′-^{3}H] KIEs of *H. pylori*, *S. aureus*, and *K. pneumoniae* MTANs were determined by the competitive radiolabeled method described previously (*4, 5, 23*). Briefly, MTAN-catalyzed hydrolyzis was carried out at 25 °C in a buffer containing 100 mM HEPES buffer (pH = 7.5), 50 mM KCl, 250 μM MTA (final concentration), and 1–5 nM MTAN. V_{max}/K_m [4′-^{3}H] and [1′-^{3}H] KIEs were measured with [5′-^{14}C]MTA as remote control, and [1′-^{14}C] KIE was determined with [4′-^{3}H]MTA as remote control. The experimental [1′-^{14}C] KIE was then subject to the correction of the remote [4′-^{3}H] KIE. Each assay was performed in a total volume of 250 μL containing at least 5×10^4 cpm for ^{14}C-labeled MTA and 3:1 for ^{3}H:^{14}C cpm. A 50-μL portion of the reaction mixture was allowed to reach 100% completion upon adding another 1 μM enzyme, and the remaining 200 μL of the reaction mixture went to 20–30% completion. These reaction mixtures were then loaded onto charcoal-cellulose columns (4:1, 100 mg total, preequilibrated with 1 mM methylthioribose) followed by washing with 1 vol of 1 mM methylthioribose. The radioactive methylthioribose was eluted with 4 vol of 15 mM methylthioribose containing 50% ethanol (v/v). The eluate was collected, dried by speedvac, and dissolved in 200 μL of water and 10 mL of scintillation fluid. The samples were then counted for 6 cycles at 10 min per cycle (Wallac 1414 LSC, PerkinElmer) and averaged. Five replicates were performed for each KIE measurement. The ^{3}H:^{14}C ratios were determined for the partial and complete reactions as described previously, and the KIEs were corrected for 0% reaction according to the following equation:

$$\text{KIE} = \frac{\ln(1-f)}{\ln\left(1 - f \times \frac{R_f}{R_0}\right)}$$

where f is the fraction of reaction completion, determined by dividing the counts in the partial reaction by the total number of counts in the full conversion reaction, and R_f and R_0 are ratios of heavy to light isotope at partial and 100% completion of reaction, respectively.

Acknowledgment: This work was supported by NIH Research Grant GM 41916.

REFERENCES

1. Wolfenden, R., and Snider, M. J. (2001) The depth of chemical time and the power of enzymes as catalysts, *Acc. Chem. Res. 34*, 938–945.
2. Schramm, V. L. (2005) Enzymatic transition states and transition state analogues, *Curr. Opin. Struct. Biol. 15*, 604–613.
3. Schramm, V. L. (2005) Enzymatic transition states: thermodynamics, dynamics and analogue design, *Arch. Biochem. Biophys. 433*, 13–26.
4. Singh, V., and Schramm, V. L. (2007) Transition-state analysis of *S. pneumoniae* 5′-methylthioadenosine nucleosidase, *J. Am. Chem. Soc. 129*, 2783–2795.

5. Singh, V., Lee, J. E., Nunez, S., Howell, P. L., and Schramm, V. L. (2005) Transition state structure of 5′-methylthioadenosine/*S*-adenosylhomocysteine nucleosidase from *Escherichia coli* and its similarity to transition state analogues, *Biochemistry 44*, 11647–11659.
6. Lewandowicz, A., and Schramm, V. L. (2004) Transition state analysis for human and *Plasmodium falciparum* purine nucleoside phosphorylases, *Biochemistry 43*, 1458–1468.
7. Kline, P. C., and Schramm, V. L. (1993) Purine nucleoside phosphorylase. Catalytic mechanism and transition-state analysis of the arsenolysis reaction, *Biochemistry 32*, 13212–13219.
8. Nikolic-Hughes, I., Rees, D. C., and Herschlag, D. (2004) Do electrostatic interactions with positively charged active site groups tighten the transition state for enzymatic phosphoryl transfer? *J. Am. Chem. Soc. 126*, 11814–11819.
9. Kim, K., and Cole, P. A. (1998) Kinetic analysis of a protein tyrosine kinase reaction transition state in the forward and reverse directions, *J. Am. Chem. Soc. 120*, 6851–6858.
10. Luo, M., Singh, V., Taylor, E. A., and Schramm, V. L. (2007) Transition-state variation in human, bovine, and *Plasmodium falciparum* adenosine deaminases, *J. Am. Chem. Soc. 129*, 8008–8017.
11. Merkler, D. J., Kline, P. C., Weiss, P., and Schramm, V. L. (1993) Transition-state analysis of AMP deaminase, *Biochemistry 32*, 12993–13001.
12. Cleland, W. W. (2005) The use of isotope effects to determine enzyme mechanisms, *Arch. Biochem. Biophys. 433*, 2–12.
13. Rodgers, J., Femec, D. A., and Schowen, R. L. (1982) Isotopic mapping of transition-state structural features associated with enzymic catalysis of methyl transfer, *J. Am. Chem. Soc. 104*, 3263–3268.
14. Anderson, V. E. (1991) Isotope effects on enzyme-catalyzed β-eliminations. In *Enzyme Mechanisms from Isotope Effects* (Cook, P. F., Ed.) pp 389–418, CRC, Boca Raton, FL.
15. Schauder, S., Shokat, K., Surette, M. G., and Bassler, B. L. (2001) The LuxS family of bacterial autoinducers: biosynthesis of a novel quorum-sensing signal molecule, *Mol. Microbiol. 41*, 463–476.
16. Withers, H., Swift, S., and Williams, P. (2001) Quorum sensing as an integral component of gene regulatory networks in Gram-negative bacteria, *Curr. Opin. Microbiol. 4*, 186–193.
17. Basu, I., Cordovano, G., Das, I., Belbin, T. J., Guha, C., and Schramm, V. L. (2007) A transition state analogue of 5′-methylthioadenosine phosphorylase induces apoptosis in head and neck cancers, *J. Biol. Chem. 282*, 21477–21486.
18. Evans, G. B., Furneaux, R. H., Lenz, D. H., Painter, G. F., Schramm, V. L., Singh, V., and Tyler, P. C. (2005) Second generation transition state analogue inhibitors of human 5′-methylthioadenosine phosphorylase, *J. Med. Chem. 48*, 4679–4689.
19. Evans, G. B., Furneaux, R. H., Schramm, V. L., Singh, V., and Tyler, P. C. (2004) Targeting the polyamine pathway with transition-state analogue inhibitors of 5′-methylthioadenosine phosphorylase, *J. Med. Chem. 47*, 3275–8281.
20. Harasawa, H., Yamada, Y., Kudoh, M., Sugahara, K., Soda, H., Hirakata, Y., Sasaki, H., Ikeda, S., Matsuo, T., Tomonaga, M., Nobori, T., and Kamihira, S. (2002) Chemotherapy targeting methylthioadenosine phosphorylase (MTAP) deficiency in adult T cell leukemia (ATL), *Leukemia 16*, 1799–1807.
21. Parsek, M. R., Val, D. L., Hanzelka, B. L., Cronan, J. E., and Greenberg, E. P. (1999) Acyl homoserine-lactone quorum-sensing signal generation, *Proc. Natl. Acad. Sci. U.S.A. 96*, 4360–4365.
22. Singh, V., Shi, W. X., Almo, S. C., Evans, G. B., Furneaux, R. H., Tyler, P. C., Painter, G. F., Lenz, D. H., Mee, S., Zheng, R. J., and Schramm, V. L. (2006) Structure and inhibition of a quorum sensing target from Streptococcus pneumoniae, *Biochemistry 45*, 12929–12941.
23. Singh, V., and Schramm, V. L. (2006) Transition-state structure of human 5′-methylthioadenosine phosphorylase, *J. Am. Chem. Soc. 128*, 14691–14696.
24. Singh, V., Evans, G. B., Lenz, D. H., Mason, J. M., Clinch, K., Mee, S., Painter, G. F., Tyler, P. C., Furneaux, R. H., Lee, J. E., Howell, P. L., and Schramm, V. L. (2005) Femtomolar transition state analogue inhibitors of 5′-methylthioadenosine/*S*-adenosylhomocysteine nucleosidase from *Escherichia coli*, *J. Biol. Chem. 280*, 18265–18273.
25. Birck, M. R., and Schramm, V. L. (2004) Nucleophilic participation in the transition state for human thymidine phosphorylase, *J. Am. Chem. Soc. 126*, 2447–2453.
26. Northrop, D. B. (1975) Steady-state analysis of kinetic isotope effects in enzymic reactions, *Biochemistry 14*, 2644–2651.
27. Lee, J. E., Singh, V., Evans, G. B., Tyler, P. C., Furneaux, R. H., Cornell, K. A., Riscoe, M. K., Schramm, V. L., and Howell, P. L. (2005) Structural rationale for the affinity of pico- and femtomolar transition state analogues of *Escherichia coli* 5′-methylthioadenosine/*S*-adenosylhomocysteine nucleosidase, *J. Biol. Chem. 280*, 18274–18282.
28. Singh, V., Shi, W., Evans, G. B., Tyler, P. C., Furneaux, R. H., Almo, S. C., and Schramm, V. L. (2004) Picomolar transition state analogue inhibitors of human 5′-methylthioadenosine phosphorylase and X-ray structure with MT-immucillin-A, *Biochemistry 43*, 9–18.
29. Luo, M., Fadeev, E. A., and Groves, J. T. (2005) Membrane dynamics of the amphiphilic siderophore, acinetoferrin, *J. Am. Chem. Soc. 127*, 1726–1736.
30. Taylor Ringia, E. A., Tyler, P. C., Evans, G. B., Furneaux, R. H., Murkin, A. S., and Schramm, V. L. (2006) Transition state analogue discrimination by related purine nucleoside phosphorylases, *J. Am. Chem. Soc. 128*, 7126–7127.
31. McCann, J. A. B., and Berti, P. J. (2007) Transition state analysis of acid-catalyzed dAMP hydrolysis, *J. Am. Chem. Soc. 129*, 7055–7064.
32. Singh, V., Luo, M., Brown, R. L., Norris, G. E., and Schramm, V. L. (2007) Transition state structure of *Neisseria meningitides* 5′methylthioadenosine/*S*-adenosylhomocysteine nucleosidase. *J. Am. Chem. Soc.*, in press